Constitutive analysis and hot deformation behavior of fine-grained Mg–Gd–Y–Zr alloys

R. ALIZADEH[a], R. MAHMUDI[a,*], O.A. RUANO[b], A.H.W. NGAN[c]

[a]*School of Metallurgical and Materials Engineering, College of Engineering, University of Tehran, Tehran, Iran*

[b]*Department of Physical Metallurgy, CENIM-CSIC, Av. Gregorio del Amo 8, 28040 Madrid, Spain*

[c]*Mechanical Engineering Department, The University of Hong Kong, Pokfulam Road, Hong Kong*

Mg–Gd–Y–Zr alloys are among the newly developed magnesium alloys with superior strength properties at elevated temperatures. Accordingly, the hot shear deformation behavior of fine-grained extruded Mg–9Gd–4Y–0.4Zr (GWK940), Mg–5Gd–4Y–0.4Zr (GWK540) and Mg–5Gd–0.4Zr (GK50) alloys was investigated using the localized shear punch testing (SPT) method. Shear punch tests were performed at 573, 623, 673, 723 and 773 K (300, 350, 400, 450 and 500 ^{o}C) under shear strain rates in the range of 6.7×10^{-3} to 6.7×10^{-2} s^{-1}. The new fitting method of Rieiro, Carsi and Ruano (RCR) was used for direct calculation of the Garofalo constants. It was concluded that that the Garofalo equation can be used satisfactorily for describing the deformation behavior of the alloys in the entire studied ranges of strain rates and temperatures. In addition, stability maps were obtained by calculations based on the Lyapunov criteria using the Garofalo constants. The predicted stability ranges of temperature and strain rate were similar for the studied alloys. At an intermediate strain rate of 0.05 s^{-1}, the optimal temperature at which a stable region is expected was found to be 648 to 673 K (375 to 400ºC) for all three materials. The most pronounced effect of the Gd and Y elements was to enhance the high temperature strength of the alloys.

Keywords: Constitutive analysis; Hot deformation; Mg–Gd–Y–Zr alloys; Shear punch testing; Stability maps

*Corresponding author: e-mail: mahmudi@ut.ac.ir, Phone: +98 21 8208 4137, Fax: +98 21 8800 6076

I. INTRODUCTION

Despite several advantages such as low density and high specific strength, magnesium and conventional Mg–Al–Zn alloys suffer from poor strength properties at elevated temperatures. Accordingly, attempts have been made to improve high temperature mechanical properties of Mg alloys by the addition of alloying elements. Among different alloying elements, it has been reported that rare-earth (RE) elements can greatly enhance high temperature stability of Mg alloys.[1,2] Mg–Gd alloys are among the newly developed Mg–RE based alloys with superior strength properties [3] and creep resistance.[4] Additionally, these alloys have shown great capability for superplasticity in both fine- [5–7] and nano-grained conditions.[8,9] Accordingly, it would be valuable to evaluate the hot deformation behavior of these alloys to further reveal the underlying mechanisms which enhance the high temperature strength properties of the Mg–Gd alloys.

There are different models and equations for describing the hot deformation behavior of metallic alloys.[10] In this regard, the hot deformation behavior of several Mg–Gd alloys has been the subject of some studies in recent years. A brief outline of some of these investigations is given in Table I[11–18], to summarize the available data in the literature. In this table, the thermo-mechanical processes and obtained grain sizes, where given, are listed in columns 2 and 3, respectively, the compression test conditions are listed in columns 4 and 5, and the constants of the Garofalo constitutive equation, which would be introduced in the following parts, are listed in columns 6–9. It is apparent from Table I that while all of these investigations have studied hot compression behavior of different Mg–xGd–yY–zZr alloys, where x, y and z are in the ranges of 7–11, 2–5 and 0.3–1.0, respectively, the effects of Gd and

Y content on the hot deformation of these alloys have not been studied in one single comprehensive work. Another important point which can be deduced from Table I is that only two papers [15,18] have studied the hot deformation behavior of the Mg–Gd–Y–Zr alloys in the wrought condition, while the other papers have focused mainly on the cast condition. Therefore, it would be valuable to investigate the effects of Gd and Y contents on the hot workability of some wrought Mg–Gd–Y–Zr alloys.

While hot compression testing is the conventional procedure for hot deformation studies, investigation of hot deformation of metallic alloys by localized testing techniques, which need only small amount of materials, is of great interest. Recently, the shear punch testing (SPT) method has successfully been used for the evaluation of hot deformation of some Mg alloys through constitutive analysis.[19–21] It is, therefore, the aim of this paper to study the hot shear deformation behavior of the fine-grained extruded Mg–Gd–Y–Zr alloys, with different Gd and Y contents, by using SPT through constitutive analysis and stability maps.

II. EXPERIMENTAL

The Mg–9 wt pct Gd–4 wt pct Y–0.4 wt pct Zr (GWK940), Mg–5 wt pct Gd–4 wt pct Y–0.4 wt pct Zr (GWK540) and Mg–5 wt pct Gd–0.4 wt pct Zr (GK50) alloys were prepared from high purity Mg and Mg–30Gd, Mg–30Y and Mg–30Zr master alloys. The melting process was conducted in an electric furnace under a protective flux cover. The molten materials were poured into a steel die preheated to 573 K (300 ^{o}C) using a tilt-casting system

77 to minimize casting defects and any melt turbulence. The extrusion process was performed at
78 673 K (400 ^{o}C) to a diameter of 10 mm using an extrusion ratio of 19:1.
79
80 The microstructural characterization of the studied alloys was performed by a Hitachi S-
81 3400N variable pressure scanning electron microscope (SEM) and a Hitachi S-4800 field
82 emission gun scanning electron microscope (FEGSEM). An acetic-picral solution was used
83 for etching. A LEO 1530 scanning electron microscope equipped with electron backscattered
84 diffraction (EBSD) detector (Oxford Nordlys nano detector with Aztec HKL, HKL
85 CHANNEL 5 acquisition and data processing software) was used for studying grain
86 orientation maps. Sample preparation for EBSD involved grinding with SiC papers, polishing
87 with diamond paste, and then vibratory polishing with an alcohol-based alumina suspension.
88
89 The hot shear deformation behavior of the alloys was assessed using the SPT method,
90 where full details are given earlier.[22] Sample preparation for SPT involves cutting thin slices
91 of about 0.9 mm thickness by the electro-discharge machining (EDM) perpendicular to the
92 extrusion direction (ED). Both sides of the disks were ground with SiC abrasive paper (grade
93 800) to a thickness of about 0.70 ± 0.05 mm in order to remove any surface roughness.
94 Prepared samples were placed inside a SPT fixture with a 2.957 mm diameter flat cylindrical
95 punch and 3.044 mm diameter receiving hole. In this way, the shear deformation is locally
96 performed at a radius of ~1.5 mm from the center of the SPT disks. The load required to
97 deform the sample, F, was measured automatically as a function of the punch displacement
98 and the data were recorded by appropriate software to determine the shear stress, τ, on the
99 tested material using the relationship[23]

$$\tau = \frac{F}{\pi D t} \quad (1)$$

where t is the specimen thickness and D is the average of the punch and die hole diameters. The SPT curves were then plotted as shear stress against normalized punch displacement. The shear punch tests were performed at temperatures of 573, 623, 673, 723 and 773 K (300, 350, 400, 450 and 500 ^{o}C) under constant cross head speeds in the range of 0.02–0.20 mm/min, corresponding to initial shear strain rates in the range of 6.7×10^{-3} to 6.7×10^{-2} s^{-1} using a screw-driven MTS testing system equipped with a three-zone split furnace. The microstructures of some SPT samples were studied by SEM after shear deformation. For this, the deformed SPT samples were cut to halves by the EDM. A schematic presentation of the deformed SPT sample after cutting is given in Figure 1, showing different areas of the SPT sample after hot shear deformation.

III. RESULTS AND DISCUSSION

A. *Microstructural Observations Before SPT*

To analyze the microstructural evolutions during hot deformation, it is first essential to characterize the pre-deformation microstructures of the studied alloys. Accordingly, the initial microstructures of the alloys in the transverse direction (TD) are shown in Figure 2. As can be observed in this figure, the microstructures of the as-extruded alloys consist of fine equiaxed recrystallized grains, with no indications of elongated grains remained in the deformed un-recrystallized state. This shows that complete dynamic recrystallization (DRX) has occurred during the extrusion process. Comparing the microstructures of the three alloys given in Figure 2, it is evident that the GWK540 and GK50 alloys have finer microstructures in

comparison with the GWK940 alloy. Average grain sizes of about 10.0 ± 0.2, 5.0 ± 0.2 and 6.0 ± 0.2 μm were calculated for the GWK940, GWK540 and GK50 alloys, respectively.

Another important feature which can be deduced from Figure 2 is the presence of fine cuboidal particles in the microstructure of the alloys. The chemical composition and crystal structure of these particles have been studied in detail in our previous publications on these alloys,[2,7–9] where it was shown that these particles have a face centered cubic (fcc) crystal structure with a lattice parameter in the range of 0.52–0.56 nm. Also, the chemical compositions of these particles were in the range of $Mg_3(Gd,Y)$ to $Mg(Gd,Y)_5$ for the GWK940 and GWK540 alloys, and close to $MgGd_2$ for the GW50 alloy.[24] For a better representation of the recrystallized microstructure of the alloys, the grain orientation map of the GWK940 alloy in the TD obtained by the EBSD method is shown in Figure 3. As can be seen in this figure, fine recrystallized grains, separated by high angle grain boundaries, are present in the microstructure of the alloy, indicating that the temperature of the extrusion process and the imposed strain and strain rate were all adequate for complete DRX of the alloys.

B. *SPT Results*

The hot deformation behavior of the alloys was studied by the shear punch testing method. The stress-displacement curves obtained at 673 K (400 ^{o}C) and under different strain rates are presented in Figure 4. Similar curves were obtained at the other test temperatures. As can be observed in this figure, SPT curves are similar to those usually obtained by the tensile

testing method. Ultimate shear strength (USS) values at each specific temperature and strain rate can be calculated from such curves. The relation between strain rate, test temperature and stress would be studied by the constitutive analysis in the following section.

C. *Flow Stress Behavior and Constitutive Equations*

It has been shown in our previous works[19,20] that the power-law equation may be used to describe the relation between shear strain rate ($\dot{\gamma}$), absolute test temperature (T) and shear stress (τ):

$$\dot{\gamma} = A\tau^{n} \exp\left(\frac{-Q}{RT}\right) \qquad (2)$$

where A is a material constant, n is the stress exponent, Q is the activation energy of deformation, and R is the universal gas constant. According to this equation, the stress exponent, n, can be calculated at each temperature by plotting the stress against strain rate on a log-log scale. These plots together with the calculated n-values are shown in Figure 5 for the three studied alloys. From the results given in Figures 4 and 5, it can be deduced that the GWK940 alloy, at all test temperatures, is slightly stronger than the GWK540 alloy, which itself is stronger than the GK50 alloy. Regarding the stress exponents, a large variation in n-values is observed with increasing temperature. The calculated stress exponents were in the ranges of 3.3–9.4, 3.4–8.9 and 2.6–7.6 for the GWK940, GWK540 and GK50 alloys, respectively. The obtained low values of stress exponent at the highest three temperatures might be considered as a sign of the possible operation of the grain boundary sliding (GBS) as the controlling mechanism of deformation, especially by considering the fine grain sizes of the

studied materials. However, this conclusion seems to be more reasonable after calculation of the activation energy values, since stress exponent itself would not be enough for concluding the operative deformation mechanisms.

The observed large variations in stress exponent values with test temperature means that the activation energy values that can be obtained from the experimental data are meaningless due to their strong dependency on the stress exponent. Therefore, it can be concluded that a complete analysis at all the temperatures shown in Figure 5 cannot be based on Eq. (2) as a consequence of the strong variation in n with temperature. Instead, the obtained results at different test temperatures can be analyzed by using a sine hyperbolic equation or the Garofalo equation[25] that describes the creep behavior of materials in wider ranges of temperatures and strain rates than the power-law equation. This equation has the form of:

$$\dot{\gamma} = A'[\sinh(\alpha\tau)]^{n'}\exp(\frac{-Q'}{RT}) \quad (3)$$

where A', α, $n'$and $Q'$are all material parameters, also called the Garofalo parameters. This equation is extensively employed in the literature to describe the flow behavior of different materials, including Mg–Gd alloys as shown in Table I. However, it should be noted that the association of the Garofalo equation parameters with usual deformation mechanisms at high temperature is different from that involving the power-law equation. This means that the activation energy or the stress exponent for both types of equations should not necessarily be the same.

Different methods have been used in the literature for determination of the Garofalo parameters. In the present work, determination of the Garofalo parameters is carried out by means of the Rieiro-Carsí-Ruano (RCR) method described elsewhere.[26] In contrast to the traditional methods, the RCR method is an improvement without the use of initial values providing, additionally, statistical parameters to quantify the goodness of the fit. The Garofalo equations obtained by the RCR method for the three studied materials are:

- GWK940: $$\dot{\gamma} = 6.477 \times 10^{9} \times [sinh(0.01758 \times \tau)]^{2.451} \times e^{\frac{-149116\ J/mol}{R \cdot T}} \quad (4)$$
- GWK540: $$\dot{\gamma} = 1.816 \times 10^{9} \times [sinh(0.01522 \cdot \tau)]^{2.466} \times e^{\frac{-138172\ J/mol}{R \cdot T}} \quad (5)$$
- GK50: $$\dot{\gamma} = 9.513 \times 10^{10} \times [sinh(0.0267 \cdot \tau)]^{2.502} \times e^{\frac{-165594\ J/mol}{R \cdot T}} \quad (6)$$

Figure 6 shows the results of the Garofalo analysis of the three materials to determine the truthfulness of the fits. In this figure, the Zener-Hollomon parameter, $Z = \dot{\gamma} \times \exp(Q'/RT)$, is plotted as a function of the $\sinh(\alpha\tau)$ on a log-log scale. It is shown in this figure that the fits are very good with correlation R^2-values in the range of 0.986–0.993, which seems acceptable. It is, therefore, concluded that the Garofalo equation can be used satisfactorily for describing the deformation behavior of the three studied fine grain alloys in the entire range of strain rates and temperatures.

A comparison of the Garofalo constants of the studied alloys presented in Eqs. 4 to 6 with those reported earlier for similar alloys in the literature (summarized in Table I) demonstrates distinct differences. While activation energies in the range of 209 to 309 kJ/mol have been reported in the literature, the obtained activation energies in this study were in the range of 138–165 kJ/mol. Additionally, larger α-values were obtained in the present study. In

addition to different testing conditions, including deformation mode, test temperature and strain rate, other variables such as the initial state of the material (cast or wrought) and also the calculation method used for obtaining the Garofalo constants may result in the observed differences.

The Garofalo equation was originally developed to generalize the creep behavior of materials in a wide range of strain rates, where the dominant creep mechanism is dislocation creep showing a stress exponent of about 5 at low stresses and increasing values of n with increasing deformation rates above the so called power-law breakdown region.[27,28] Surprising is, therefore, the low stress exponents of about 2.0 to 2.5 found in this study according to the Garofalo equation. These low stress exponents at low strain rates used to be associated with a grain boundary sliding mechanism and superplasticity in fine grain materials as those investigated in this work. The constitutive equation usually used to describe grain boundary sliding in materials is a power-law of the type[29]

$$\dot{\varepsilon} = \mathrm{K}\left(\frac{\sigma}{\mathrm{E}}\right)^{2}\left(\frac{\mathrm{b}}{\mathrm{L}}\right)^{\mathrm{p}}\exp\left(-\frac{\mathrm{Q}}{\mathrm{RT}}\right) \quad (7)$$

where $\dot{\varepsilon}$ is the strain rate, K is a constant, L is the grain size, b is the Burger vector, E is Young's modulus and p is the grain size exponent. While the stress exponent of the power-law equation, n, is considered to be about 2 for the GBS mechanism at the entire range of temperatures, different combinations of the Q and p parameters have been assumed depending on the temperature of deformation. In this regard, values of $p = 3$ and $Q = Q_{gb}$ at $0.4T_m < T < 0.6T_m$, while for $T > 0.6T_m$, $p = 2$ and $Q = Q_L$ (Q_{gb} and Q_L are the activation energy values for grain boundary and lattice diffusion, respectively, and T_m is absolute melting temperature) are used. Accordingly, Eq. (7) predicts that the finer is the grain size, the higher is the strain rate

234 and the lower is the temperature at which GBS can operate. This was shown in our previous
235 work for the GWK940 alloy, where reducing the grain size from about 8.6 μm in the extruded
236 condition to less than 95 nm after high pressure torsion (HPT) resulted in about 100 K
237 decrease in the optimum temperature for the operation of GBS and probable occurrence of
238 superplasticity.[8] Consequently, the fact that the Garofalo equation presents low stress
239 exponents in the studied fine-grained materials is not a surprise since this equation prioritizes
240 the low strain rate behavior for determining the stress exponent, because in the equation it
241 represents the limit of *n* values at low strain rates. It is, therefore, predicted that superplasticity
242 is taking place at these low strain rates. Furthermore, the lowest value of the strain rate, $6.7 \times$
243 10^{-3} s^{-1}, is a typical one to show grain boundary sliding. Indeed, superplasticity has certainly
244 been reported in the Mg–5 wt pct Gd–4 wt pctY–0.4 wt pct Zr alloy[9] attesting the validity of
245 the method in detecting grain boundary sliding at some strain rates.
246
247 Now, the question is that if the Garofalo equation may describe grain boundary sliding
248 in fine grained materials as a substitute of the power-law equation, Eq. (7), for a wider range
249 of strain rates. It should be noted that in the case of ultrafine grains of less than 1 micron, the
250 grain boundary sliding mechanism may control deformation at strain rates in excess of 10^{-1} s^{-1}.
251 This is the case of high strain rate superplasticity. Under extreme testing conditions, the stress
252 exponents and activation energies usually do not correspond to the theoretical ones according
253 to the constitutive equations ($n = 2$ and $Q = Q_L$ or Q_{gb}), which could be due to the creep
254 behavior that is leaving the grain boundary sliding range. However, superplastic elongations
255 have not been observed in samples tested at strain rate and temperature conditions where the
256 stress exponent is higher than 3. This can be checked microstructurally, since in the

257 superplastic range the shape of the grains has to be equiaxed and the texture should not be
258 reinforced after deformation.
259
260 For better examination of the possible occurrence of superplasticity in the studied
261 materials, it is better to evaluate the strain rate sensitivity (SRS) index, since superplasticity is
262 in close relation with the strain rate sensitivity of materials, providing an indirect method for
263 the identification of superplasticity. The variation of the strain rate sensitivity index, m, as a
264 function of strain rate and temperature can be deduced from the power-law stress exponents
265 presented in Figure 5, since $m = 1/n$. However, a better description of this variation can be
266 made from the evolution of m-values that can be obtained from the Garofalo equation for a
267 particular material. This is done in Figure 7 for the GWK940 alloy. Values of m between
268 0.136 and 0.388, i.e. n between 2.6 and 7.4, are observed in Figure 7, which are similar to
269 those observed for the other two materials except for lower n values at low strain rates that are
270 observed in the GK50 alloy. These values, obtained directly from the Garofalo equation, are
271 related to the values obtained through the power law equation but are not necessarily the
272 same.[30] SEM micrographs of the GWK940 alloy after SPT at 723 K (450ºC) under strain rate
273 of 3.3×10^{-2} s^{-1} are shown in Figure 8. Extensive deformation of the material in the shear
274 region can be depicted from this figure, where the thickness of the specimen has been reduced
275 to less than 10 grains. This is in accordance with superplasticity and the observed m-values of
276 the material at this temperature and strain rate, since it is usually accepted that high m-values
277 approaching ~ 0.50 may be associated with superplastic deformation and the GBS
278 mechanism.[31] Furthermore, there is no sign of elongated grains in the highly strained narrow

279 region, implying that grain boundary sliding has occurred and an equiaxed grain structure is
280 prevalent.
281
282 According to the above discussion, therefore, it is concluded that a grain boundary
283 sliding equation that involves high stress exponents at certain values of strain rates, as the
284 Garofalo equation, will not describe the superplastic behavior of materials. Although not
285 adequate to describe the behavior of GBS, this equation is valid to describe the deformation
286 behavior in a wide range of temperatures and strain rates as attested by the narrow scatter
287 observed in Figure 6. In other words, this equation would not discriminate among the most
288 well-known deformation mechanisms: diffusional flow, grain boundary sliding and slip creep,
289 but it can be used as a tool to describe the general behavior of materials including grain
290 boundary sliding as is the case of these magnesium alloys. This characteristic makes this
291 equation also appropriate to determine the stability conditions of the materials, which would
292 be studied in the following section.
293
294 **D.** *Stability of the Materials*
295 Prasad et al.[32] introduced material variables that describe the plastic flow in theoretical
296 models based on physical laws. This concept is called dynamic material model, DMM. For
297 identification of instabilities, in this work we introduce the Garofalo equation for each alloy,
298 Eqs. 4-6, directly in the Lyapunov stability principles as modeled through DMM by Gegel et
299 al.,[33] avoiding the use of a power law for reaching a stability criterion.[34,35] In the DMM, the
300 working unit of the material is assumed to be a power dissipater, P, that is divided into two
301 terms: G, the dissipator content, is the power spent in the deformation manifested in the form

of heat increment (no change in the internal structure) and J, the dissipator co-content, is the power spent in the deformation with a change of the internal structure. In this regard, two parameters are important to characterize the system; the sensitivity of the stress to the strain rate or strain rate sensitivity exponent, m, that regulates the relationship between the two contents, and the sensitivity of the stress to the temperature, s, that regulates the relationship between the two entropies, one applied to the system and the other obtained from the system. These sensitivities are defined in the experimental framework and therefore are linked to the stress-strain rate curves and not to the equations corresponding to the curves that will have different analytical shapes and differences according to the applications (power-law, Garofalo, Bingham, etc.). The expressions for m and s are as follows:

$$m = \frac{\dot{\varepsilon}}{\sigma} \cdot \frac{\partial \sigma}{\partial \dot{\varepsilon}}\Big]_{\varepsilon,T=cte.} = \frac{\partial Ln(\sigma)}{\partial Ln(\dot{\varepsilon})}\Big]_{\varepsilon,T=cte.} = \frac{dJ}{dG} \qquad 0 \le m \le 1 \tag{8}$$

$$s = \frac{\dot{S}_{sys}}{\dot{S}_{app}} = \left[\frac{1}{T} \cdot \frac{\partial Ln(\sigma)}{\partial(\frac{1}{T})}\right]_{\dot{\varepsilon}}, \; s \ge 1 \tag{9}$$

where $\dot{s}_{sys}$ is the entropy rate obtained from the system and $\dot{s}_{app}$ is that applied to the system.

On the other hand, the expressions for the dissipated contents in the process are:

$$P = \sigma \cdot \dot{\varepsilon} = G + J, \text{ where } G = \int_0^{\dot{\varepsilon}} \sigma \cdot d\dot{\varepsilon} \text{ and } J = \int_0^{\sigma} \dot{\varepsilon} \cdot d\sigma \tag{10}$$

The last basic element of DMM is the efficiency, η, of the dissipator co-content, due to the interest in the recovery and dynamic recrystallization processes, where

$$\eta = \frac{J}{J_{max}} \tag{11}$$

that is converted by Prasad, using a power-law approximation, into

$$\eta = 2m/(m+1) \tag{12}$$

Searching for other kinds of stability conditions, Gegel et al.[33] used the Lyapunov criteria, that determine stability zones, and applied them to materials. These authors used the concept of Lyapunov functions V_1 and V_2 and postulated, under the framework of DMM, that:

$$V_1 = \eta\big(log(\dot{\varepsilon})\big)\ and\ V_2 = s\big(log(\dot{\varepsilon})\big) \tag{13}$$

The function V_1 is related to energy dissipation oriented toward modification of the microstructure and V_2 is related to the production of entropy in the system, giving the following stability criteria:

$$\frac{\partial V_1}{\partial Ln(\dot{\varepsilon})} = \frac{\partial \eta}{\partial Ln(\dot{\varepsilon})} < 0$$

$$\frac{\partial V_2}{\partial Ln(\dot{\varepsilon})} = \frac{\partial s}{\partial Ln(\dot{\varepsilon})} < 0 \tag{14}$$

that the authors solved by means of a power-law approximation. This contains a fundamental contradiction since m, in the power-law, is a constant that do not varies with $\dot{\varepsilon}$ and T. Since the maps have to show variation with these two variables, the authors used small intervals of strain rates not considering that each strain rate may contain important calculation and numeric errors. Furthermore, polynomial approximations of second or third order to determine m are used. This determination is therefore strongly subject to scattering of the experimental data.

Our approximation to the stability problem and the construction of stability maps follows a different path. First we adjust all the experimental data to a hyperbolic sine equation of Garofalo type and then we calculate the m values for each $\dot{\varepsilon}$ and T. We have therefore a unique equation for all the experimental conditions that has the following form:

$$\dot{\varepsilon} = A^G \cdot e^{-\frac{Q^G}{R \cdot T}} \cdot [sinh\,(\alpha^G \cdot \sigma)]^{n_G} \quad (15)$$

where the index G means that the Garofalo equation is used. The four parameters of this equation, $\{A^G, Q^G, n^G, \alpha^G\}$ are calculated simultaneously.[26]

Introducing the Garofalo equation directly in the Lyapunov stability principles as modeled in the DMM by Gegel et al.[33], Eq. (14), the following equation is obtained:

$$\frac{\partial \eta_G}{\partial \dot{\varepsilon}} = 2\left[\frac{1}{n_G \cdot \dot{\varepsilon} \cdot \{sinh^{-1}(\theta^G)\} \cdot \sqrt{1+\theta^{G^{-2}}}} - \frac{\left\{\int_0^{\dot{\varepsilon}} \frac{d\dot{\varepsilon}}{\sqrt{1+\theta^{G^{-2}}}}\right\}}{n_G \cdot \dot{\varepsilon} \cdot \{sinh^{-1}(\theta^G)\}} \cdot \left(\frac{n_G \cdot \{sinh^{-1}(\theta^G)\}}{n_G \cdot \dot{\varepsilon} \cdot \{sinh^{-1}(\theta^G)\}} + \frac{\frac{\theta^G}{\sqrt{1+\theta^{G^2}}}}{n_G \cdot \dot{\varepsilon} \cdot \{sinh^{-1}(\theta^G)\}}\right)\right] < 0 \quad (16)$$

This new equation normalized to J/(P/2) corresponds to the first stability criterion.

Regarding the second stability criterion, from the definition of s, Eq. (9), it is obtained:

$$s^G = \left(\frac{Q}{R \cdot T}\right) \cdot \left(\frac{\theta^G}{n \cdot sinh^{-1}(\theta^G) \cdot \sqrt{1+\theta^{G^2}}}\right) \text{ where } \theta(\dot{\varepsilon}, T)^G = \left(\frac{\dot{\varepsilon} \cdot e^{\frac{Q^G}{R \cdot T}}}{A^G}\right)^{\left(\frac{1}{n_G}\right)} \quad (17)$$

and by its derivative the following stability criterion is obtained:

$$\frac{\partial s^G}{\partial Ln(\dot{\varepsilon})} = \left(\frac{Q}{R \cdot T}\right) \cdot \left(\frac{1}{{n_G}^2}\right) \cdot \left(\frac{\theta^G \cdot sinh^{-1}(\theta^G) - \theta^{G^2} \cdot \sqrt{1+\theta^{G^2}}}{\left(1+\theta^{G^2}\right)^{\frac{3}{2}} \cdot \left(sinh^{-1}(\theta^G)\right)^2}\right) < 0 \quad (18)$$

Stability maps were constructed using Eq. (18), the equations given in Eqs. (4-6) and a MATHCAD Pro 7.0 program. The Lyapunov maps for the three studied materials are given in Figure 9. Similar maps could be obtained through the use of Eq. (16) but are omitted for the sake of simplicity. The maps of Figure 9 show stability regions between the lines with minimum $\frac{\partial s^G}{\partial Ln(\dot{\varepsilon})}$ values of −1.257, −1.188 and −1.315 for the GWK940, GWK540 and GK50 alloys, respectively. These stable regions extend from low strain rates to high strain rates. At

367 an intermediate strain rate, 0.05 s^{-1} (ln(–0.05) = –3), the optimal temperature at which a
368 stable region is expected is between 648 and 673 K (375 to 400ºC) for all three materials.
369 The optimal forming temperature is not related to the creep resistance of the materials since
370 the higher optimal temperature, 673 K (400ºC), corresponds to the Mg–5Gd–0.4Zr alloy that
371 is the less creep resistant. However, the differences in optimal temperatures are relatively
372 small among the three alloys and could be attributed to the presence of a low stress exponent
373 region at low strain rates that influences the Garofalo constants.
374
375 The microstructures of the studied alloys are shown in Figure 10 after shear
376 deformation at 673 K (400 °C) and under strain rate of 3.3×10^{-2} s^{-1} (this combination of
377 temperature and strain rate seems close to the stability regions of the alloys presented in
378 Figure 9). These micrographs have been taken from the shear region of the SPT samples. As
379 can be observed in this figure, almost fully recrystallized microstructures are developed in all
380 alloys after SPT at this condition. No cracks, voids, or un-recrystallized regions can be found
381 in these micrographs, which demonstrate the compatibility of stability maps found in this
382 investigation with the real experimental results.
383
384 According to the obtained results in this investigation, it can be concluded that the hot
385 deformation behavior of the studied fine grained Mg–Gd–Y–Zr alloys with different
386 concentrations of Gd and Y does not depend significantly on the Gd and Y contents. In
387 addition to the stability maps of the alloys presented in Figure 9, this conclusion seems more
388 reasonable by comparing the microstructures of the alloys after hot deformation. In this
389 regard, it should be noted that the microstructure of the all three studied alloys after the hot

extrusion process (Figure 2) demonstrated the complete occurrence of DRX. It shows that although the studied alloys contained different concentrations of Gd and Y elements, the imposed strain during the extrusion process of the alloys at 673 K was enough for complete DRX of these alloys. Similar results were presented in Figure 10, obtained after SPT at a given test temperature and strain rate for all studied alloys. The microstructure of the tested alloys consisted of fine recrystallized grains as observed in this figure. Accordingly, it can be concluded that the hot deformation behaviors of the studied Mg–Gd–Y–Zr alloys are similar and in this regard, variations in Gd and Y contents of these alloys did not greatly change the recrystallization behavior at the investigated ranges of chemical compositions, test temperatures and strain rates. In fact, the most pronounced effect of Gd and Y contents was on the strength properties, where GWK940 alloy which contains more concentrations of RE elements in comparison with the GWK540 and GK50 alloys, presented the highest strength level among the studied alloys (Figures 4 and 5).

IV. CONCLUSIONS

The shear punch testing method was used for the evaluation of the hot deformation behavior of Mg–9Gd–4Y–0.4Zr, Mg–5Gd–4Y–0.4Zr and Mg–5Gd–0.4Zr alloys through constitutive analysis and stability maps and the following results were obtained:

1. The Garofalo equation could be used satisfactorily for describing the general behavior of the tested fine-grained alloys in the studied ranges of temperature and strain rate.

2. The obtained constants of the Garofalo equation, calculated by the RCR method, indicated possible occurrence of GBS mechanism, which was in close relation with the microstructure of the alloys after hot shear deformation.
3. All three studied alloys showed extended stability regions from low to high strain rates regions. Complete recrystallization was observed in the microstructure of the alloys after deformation within the stability regions.
4. While the Gd and Y contents did not greatly affect the recrystallization behavior of the studied alloys, their most pronounced effect was to increase the high temperature strength of the alloys. In this regard, the Mg–9Gd–4Y–0.4Zr alloys indicated the highest strength level among the investigated alloys within the studied test conditions.

Acknowledgements

The authors thank the Iran National Science Foundation (INSF) for support of this work under Grant No. 94028861. The Spanish MAT2015-68919 program is acknowledged.

REFERENCES

[1] J. Cizek, I. Prochazka, B. Smola, I. Stulikova, R. Kuzel, Z. Matej, V. Cherkaska, R.K. Islamgaliev, and O. Kulyasova: *Mater. Sci. Eng.*, 2007, vol. 462A, pp. 121–6.

[2] R. Alizadeh, R. Mahmudi, A. H. W. Ngan and T. G. Langdon: *J. Mater. Sci.*, 2015, vol. 50, pp. 4940–51.

[3] A. Movahedi-Rad and R. Mahmudi: *Mater. Sci. Eng.*, 2014, vol. 614, pp. 62–6.

[4] B.L. Mordike: *Mater. Sci. Eng.*, 2002, vol. 324, pp. 103–12.

[5] X. Zhang, L. Li, Y. Deng, and N. Zhou: *J. Alloy. Compd.*, 2009, vol. 481, pp. 296–300.

[6] R. Alizadeh, R. Mahmudi, and T.G. Langdon: *J. Mater. Res. Technol.*, 2014, vol. 3(3), pp. 228–32.

[7] R. Alizadeh, R. Mahmudi, A.H.W. Ngan, Y. Huang, and T.G. Langdon: *Metall. Mater. Trans. A*, 2016, vol. 47, pp. 6056–69.

[8] R. Alizadeh, R. Mahmudi, A.H.W. Ngan, Y. Huang, and T.G. Langdon: *Mater. Sci. Eng.*, 2016, vol. 651A, pp. 786–794.

[9] R. Alizadeh, R. Mahmudi, P.H.R. Pereira, Y. Huang, and T.G. Langdon: *Mater. Sci. Eng.*, 2017, vol. 682A, pp. 577–585.

[10] Y.C. Lin and X.-M. Chen: *Mater. Des.*, 2011, vol. 32, pp. 1733–59.

[11] Ming-long Ma, Kui Zhang, and Xing-gang Li: *Tran. Nonferrous Met. China*, 2008, vol. 18, 132–9.

[12] R. Yu, S. Wang, Q. Tang, and X. Zeng: *Mater. Sci. Forum*, 2013, vols. 747–748, 204–10.

[13] Bin Chen, Wei-Min Zhou, Song Li, Xiao-Ling Li, and Chen Lu: *J. Mater. Eng. Perform.*, 2013, vol. 22(9), pp. 2458–66.

[14] X. Xia, Q. Chen, K. Zhang, Z. Zhao, M. Ma, X. Li, and Y. Li: *Mater. Sci. Eng. A*, 2013, vol. 587, 283–90.

[15] X. Xia, Q. Chen, J. Li, D. Shu, C. Hu, S. Huang, and Z. Zhao: *J. Alloys Compd.*, 2014, vol. 610, pp. 203–11.

[16] Guang Lu, ZhipingXie, Zhimin Zhang, YongbiaoYang, and Baocheng Li: *Appl. Mech. Mater.*, 2014, vol. 680, pp 15-22.

[17] Li Li and X. Zhang: *Mater. Sci. Eng.*, 2011, vol. 528A, pp. 1396–401.

[18] H. Zhou, Q.D. Wang, B. Ye, and W. Guo: *Mater. Sci. Eng.*, 2013, vol. 576A, pp. 101–7.

[19] M. Karami and R. Mahmudi: *Mater. Des.*, 2014, vol. 53, pp. 534–539.

[20] M. Sarebanzadeh, R. Mahmudi, and R. Roumina: *Mater. Sci. Eng.*, 2015, vol. 637A, pp. 155–161.

[21] R. Alizadeh, R. Mahmudi, A.H.W. Ngan, and T.G. Langdon: *J. Mater. Sci.*, 2017, vol. 52, pp. 7843–7857.

[22] R. Mahmudi, R. Alizadeh, and Sh. Azhari: *Mater. Lett.*, 2013, vol. 97, pp. 44–46

[23] G.L. Hankin, M.B. Toloczko, K.I. Johnson, M.A. Khaleel, M.L. Hamilton, F.A. Garner, R.W. Davies, and R.G. Faulkner: *ASTM STP*, 2000, vol. 1366, pp. 1018–28.

[24] R. Alizadeh, R. Mahmudi, A.H.W. Ngan, and T.G. Langdon: *Adv. Eng. Mater.*, 2016,vol. 18 (6), pp. 1044–1049.

[25] F. Garofalo: Fundamentals of creep and creep rupture in metals, MacMillan, New York (1965).

[26] I. Rieiro, M. Carsí, and O.A. Ruano: *Mater. Sci. Technol.*, 2009, vol. 25, pp. 995–1002.

[27] O.D. Sherby and P.M. Burke: *Prog. Mater. Sci.*, 1967, vol. 13, pp. 325–390.
[28] S. Spigarelli, O.A. Ruano, M. ElMehtedi, and J.A. del Valle: *Mater. Sci. Eng.*, 2013, vol. 570A, pp. 135–148.
[29] O.A. Ruano, A.K. Miller, and O.D. Sherby: *Mater. Sci. Eng.*, 1981, vol. 51, pp. 9–16.
[30] J. Castellanos, I. Rieiro, M. Carsí, and O.A. Ruano: *J. Mater. Sci.*, 2010, vol. 45, pp. 5522–5527.
[31] T.G. Langdon: *Acta Met. Mater.*, 1994, vol. 42, pp. 2437–2443.
[32] Y.V.R.K. Prasad, H.L. Gegel, S.M. Doraivelu, J.C. Malas, J.T. Morgen, K.A. Lark, and D.R. Barker: *Metall. Trans. A*, 1984, vol. 15, pp. 1883–1892.
[33] H.L. Gegel, J.C. Malas, S.M. Doraivelu, and V.A. Shende: *Metals Handbook*, vol. 14, ASM Metals Park, 1987, p. 417.
[34] I. Rieiro, M. Carsí, and O.A. Ruano: *Mater. Sci. Forum.*, 2017, vol. 879, pp. 1618–1623.
[35] I. Rieiro, M. Carsí, and O.A. Ruano: *Metall. Mater. Trans. A*, online 04 May 2017, DOI: 10.1007/s11661-017-4102-1.

Legends

Table I. Summary of Literature Data on the Hot deformation Analysis of Mg–Gd–Y–Zr alloys

Figure 1. 3D schematic of the SPT disks after deformation, showing different areas of die, punch and deformation.

Figure 2. SEM micrographs of the GWK940 (a,b), GWK540 (c,d) and GK50 (e,f) in the TD.

Figure 3. EBSD orientation map of the GWK940 alloy in the TD.

Figure 4. SPT curves of the GWK940 (a), GWK540 (b) and GK50 (c) alloys at 673 K (400 °C) under different strain rates.

Figure 5. Shear strain rate vs. shear stress at different temperatures for the GWK940 (a), GWK540 (b) and GK50 (c) alloys.

Figure 6. The Zener-Hollomon parameter as a function of $\sinh(\alpha\tau)$ for the GWK940 (a), GWK540 (b) and GK50 (c) alloys.

Figure 7. Evolution of *m*-value of the GWK940 alloy as a function of strain rate and temperature.

Figure 8. SEM micrographs of the GWK940 alloy after SPT at 723 K (450 °C) under shear strain rate of 3.3×10^{-2} s^{-1}.

Figure 9. Stability maps corresponding to the second Lyapunov criterion for the GWK940 (a), GWK540 (b) and GK50 (c) alloys.

Figure 10. SEM micrographs from the deformation area of the GWK940 (a), GWK540 (b) and GK50 (c) alloys after SPT at 673 K (400 °C) under shear strain rate of 3.3×10^{-2} s^{-1}.

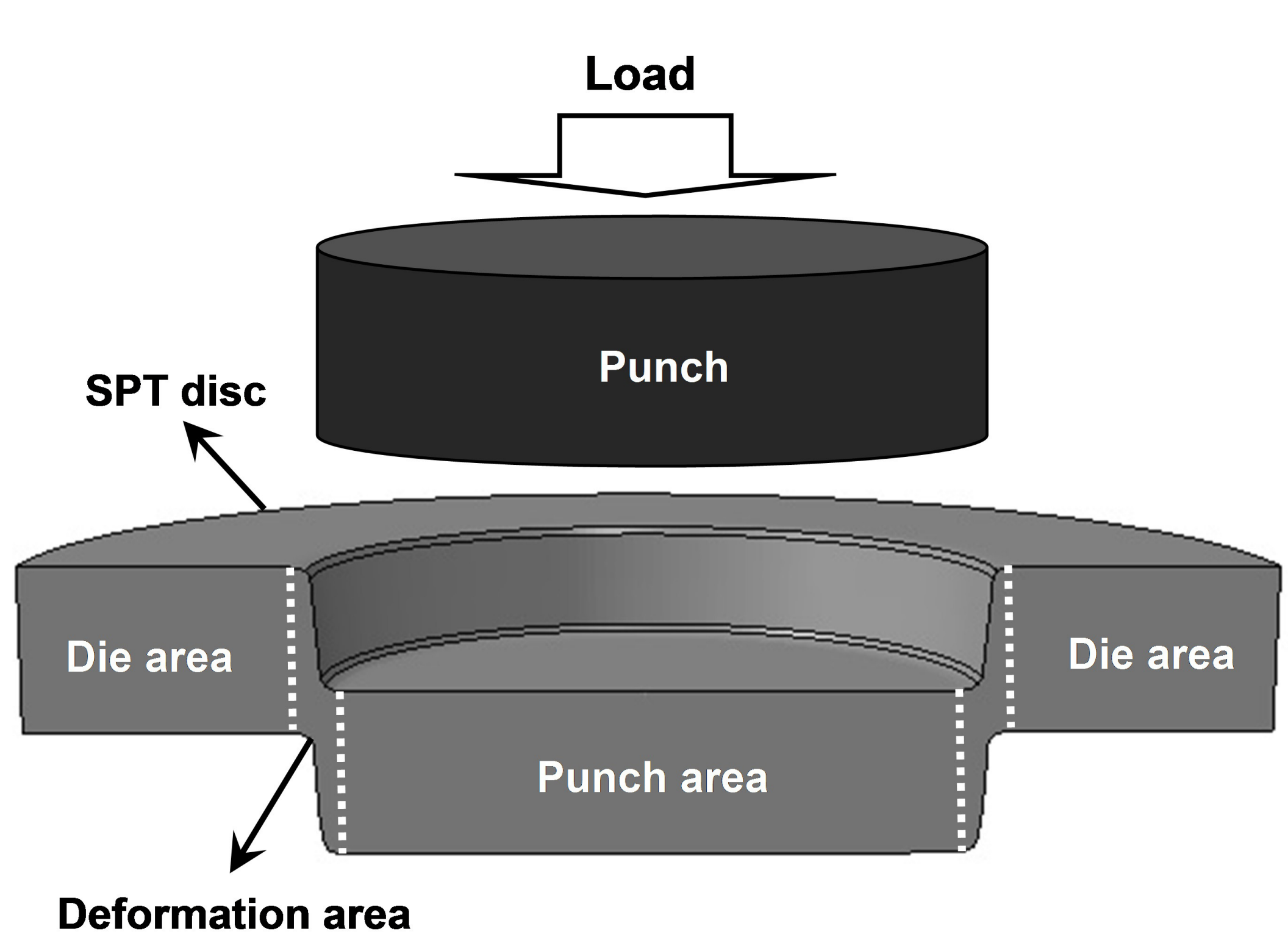
Load
Punch
SPT disc
Die area
Die area
Punch area
Deformation area

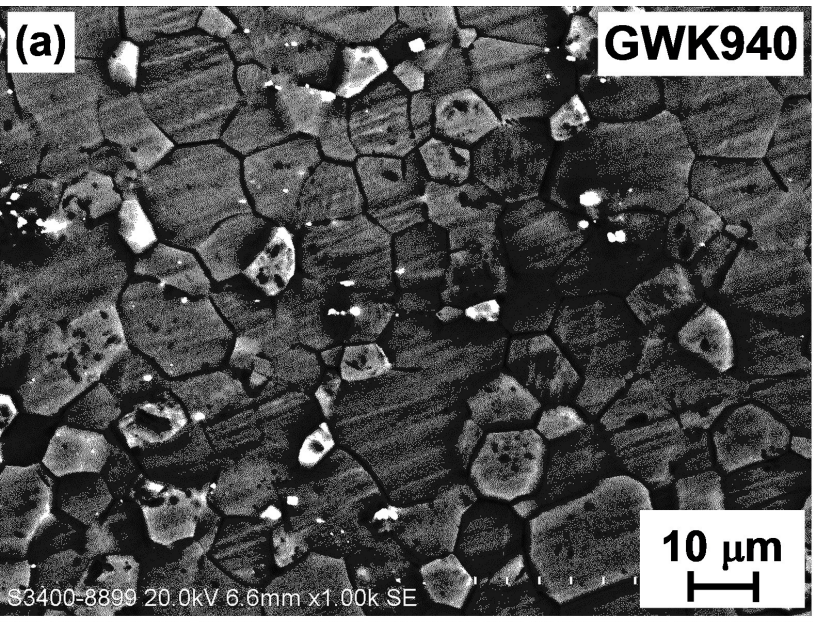
(a)
GWK940
10 μm
S3400-8899 20.0kV 6.6mm x1.00k SE

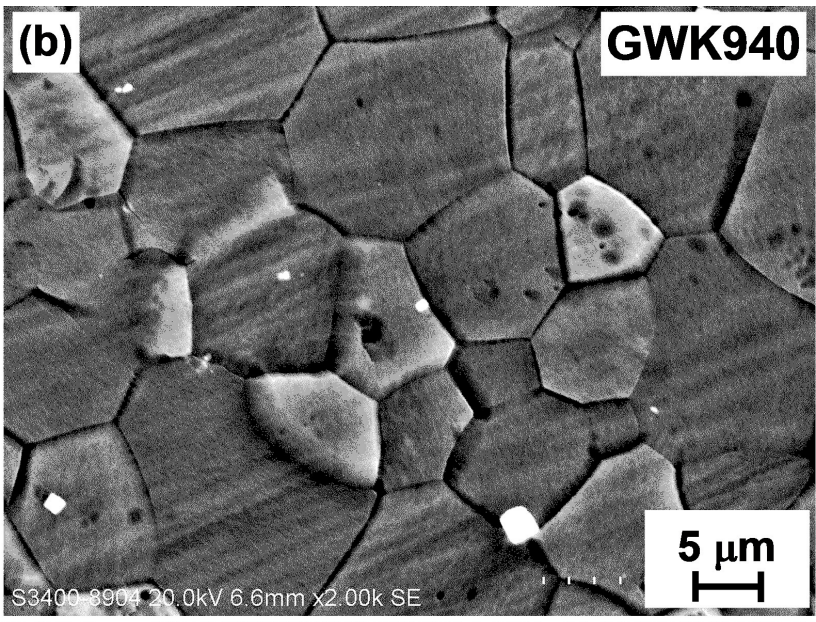
(b)
GWK940
5 μm
S3400-8904 20.0kV 6.6mm x2.00k SE

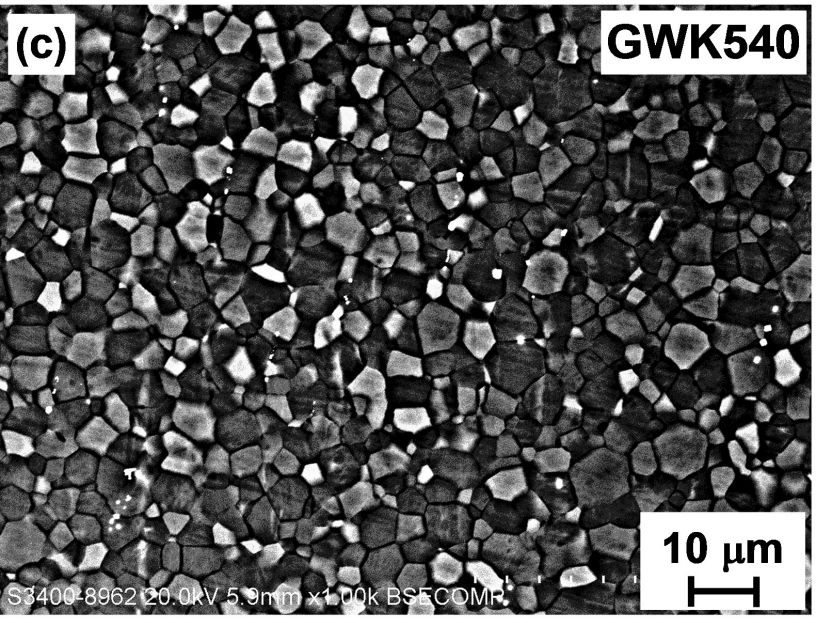
(c)
GWK540
10 μm
S3400-8962 20.0kV 5.9mm x1.00k BSECOMP

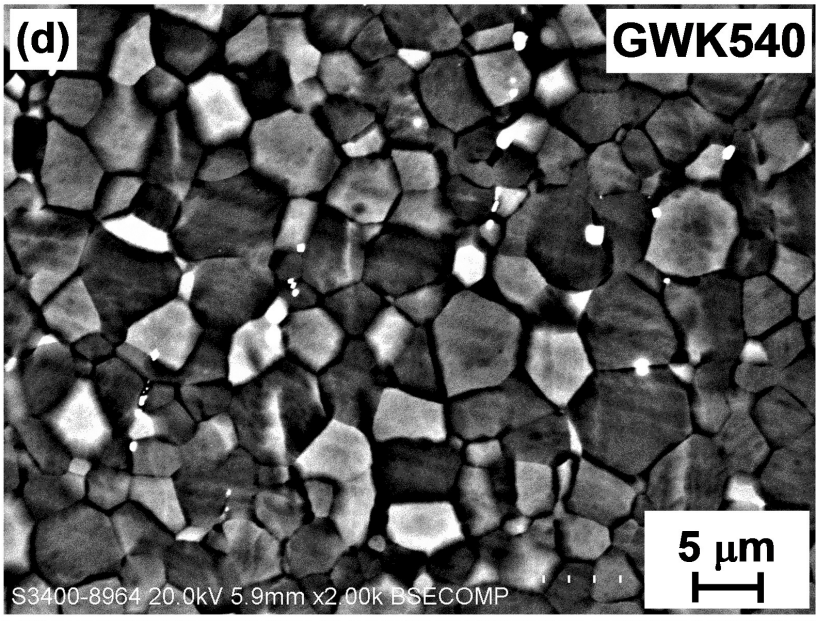
(d)
GWK540
5 μm
S3400-8964 20.0kV 5.9mm x2.00k BSECOMP

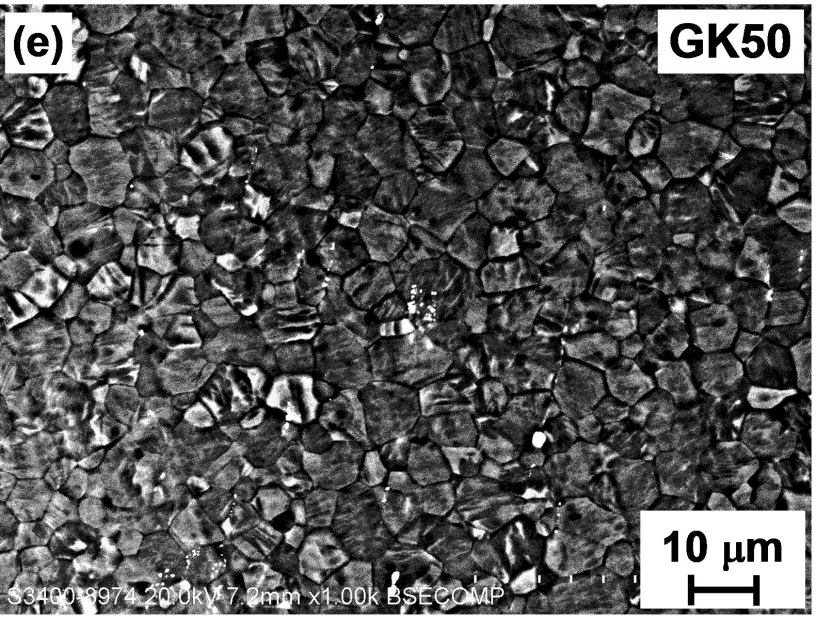
(e)
GK50
10 μm
S3400-8974 20.0kV 7.2mm x1.00k BSECOMP

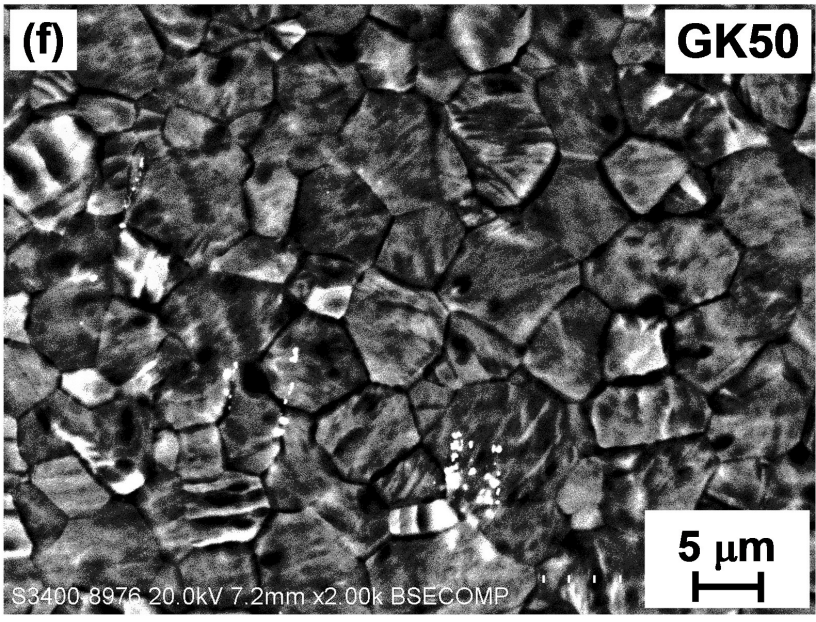
(f)
GK50
5 μm
S3400-8976 20.0kV 7.2mm x2.00k BSECOMP

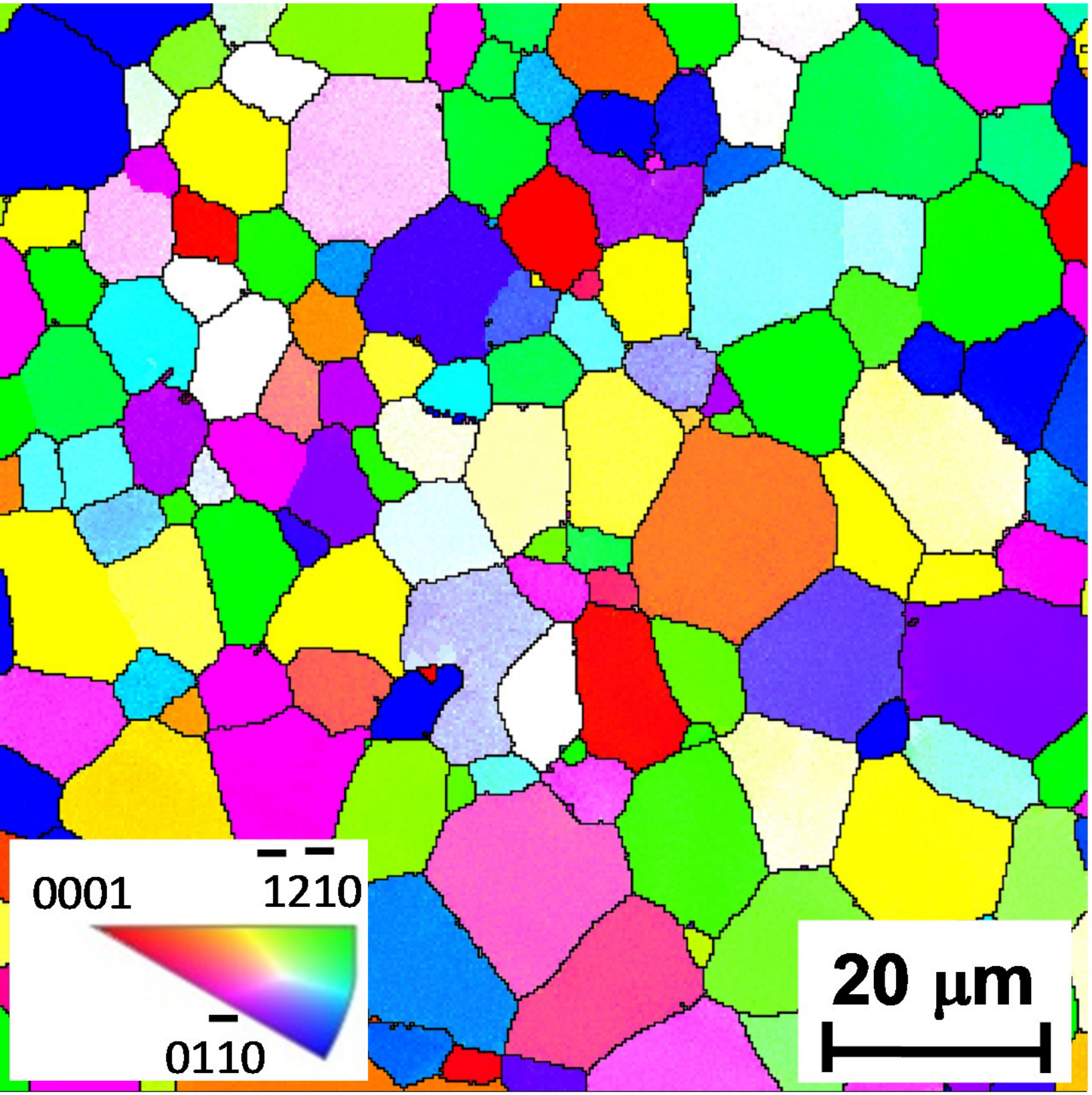
0001
$\bar{1}2\bar{1}0$
$01\bar{1}0$
20 µm

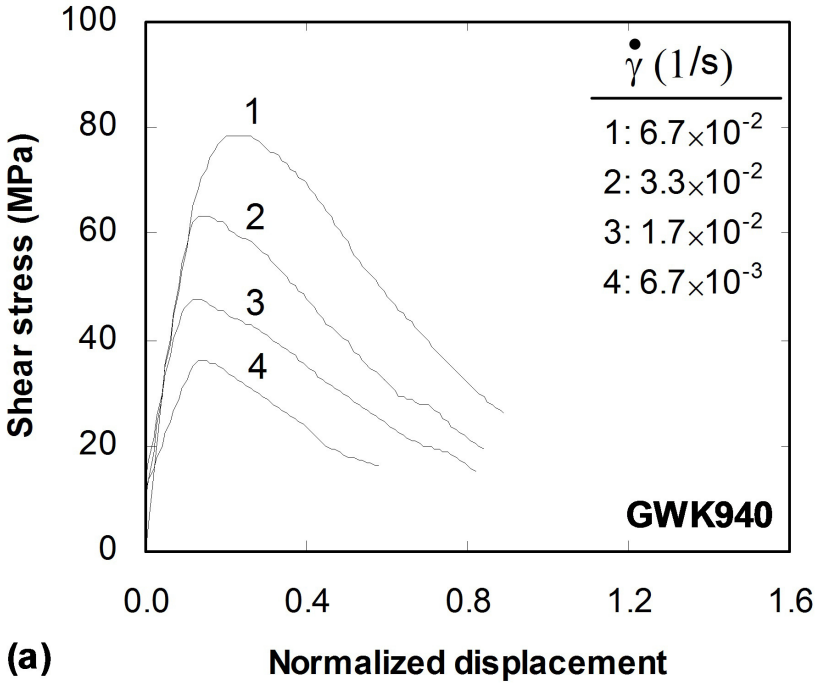
100
80
60
40
20
0
Shear stress (MPa)
$\dot{\gamma}$ (1/s)
1: 6.7×10-2
2: 3.3×10-2
3: 1.7×10-2
4: 6.7×10-3
1
2
3
4
GWK940
0.0
0.4
0.8
1.2
1.6
Normalized displacement

(a)

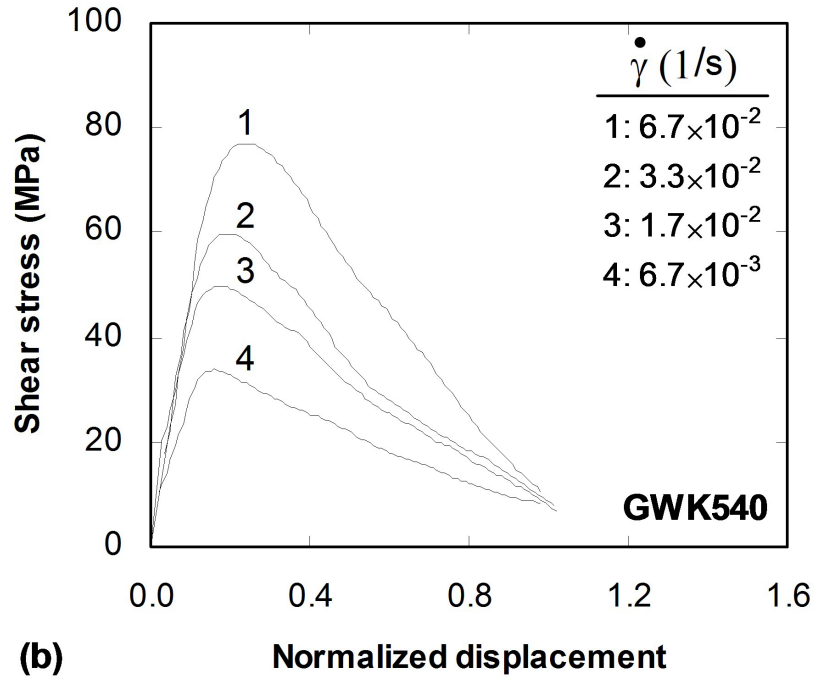
100
80
60
40
20
0
Shear stress (MPa)
$\dot{\gamma}$ (1/s)
1: 6.7×10-2
2: 3.3×10-2
3: 1.7×10-2
4: 6.7×10-3
1
2
3
4
GWK540
0.0
0.4
0.8
1.2
1.6
Normalized displacement

(b)

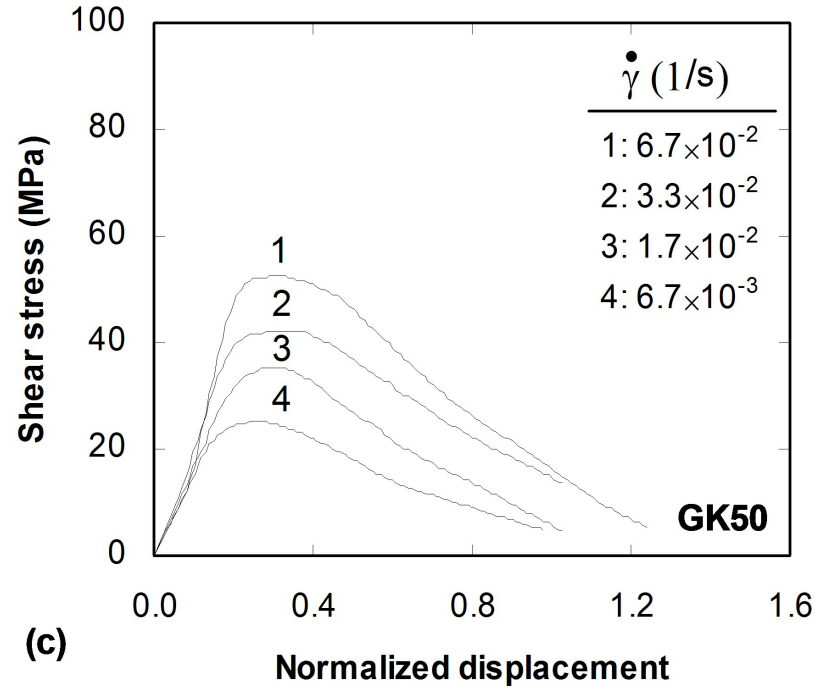
100
80
60
40
20
0
Shear stress (MPa)
$\dot{\gamma}$ (1/s)
1: 6.7×10-2
2: 3.3×10-2
3: 1.7×10-2
4: 6.7×10-3
1
2
3
4
GK50
0.0
0.4
0.8
1.2
1.6
Normalized displacement

(c)

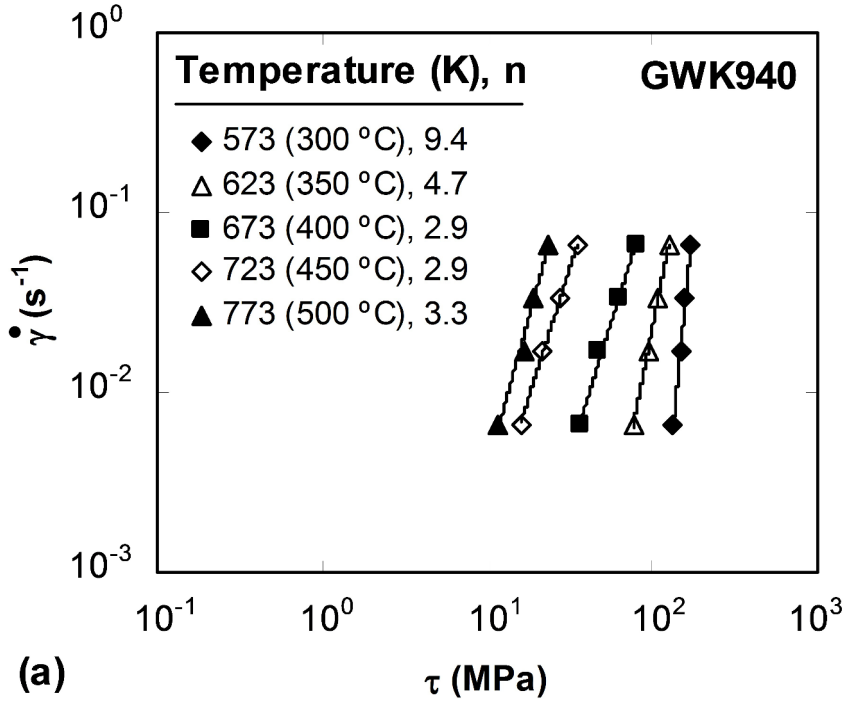
Temperature (K), n
GWK940
573 (300 °C), 9.4
623 (350 °C), 4.7
673 (400 °C), 2.9
723 (450 °C), 2.9
773 (500 °C), 3.3
$\dot{\gamma}$ (s^{-1})
10^{0}
10^{-1}
10^{-2}
10^{-3}
10^{-1}
10^{0}
10^{1}
10^{2}
10^{3}
τ (MPa)

(a)

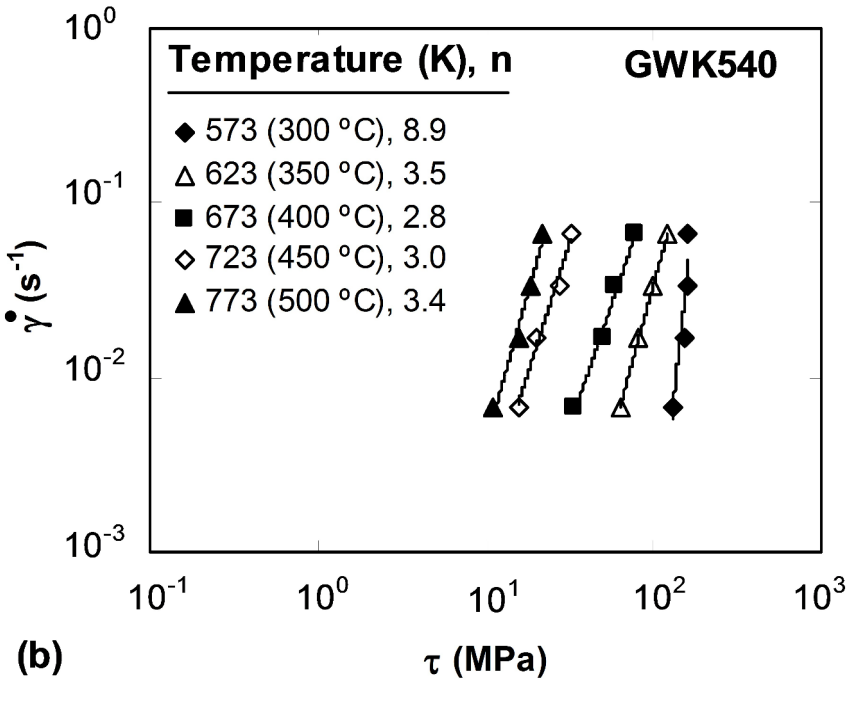
Temperature (K), n
GWK540
573 (300 °C), 8.9
623 (350 °C), 3.5
673 (400 °C), 2.8
723 (450 °C), 3.0
773 (500 °C), 3.4
$\dot{\gamma}$ (s^{-1})
10^{0}
10^{-1}
10^{-2}
10^{-3}
10^{-1}
10^{0}
10^{1}
10^{2}
10^{3}
τ (MPa)

(b)

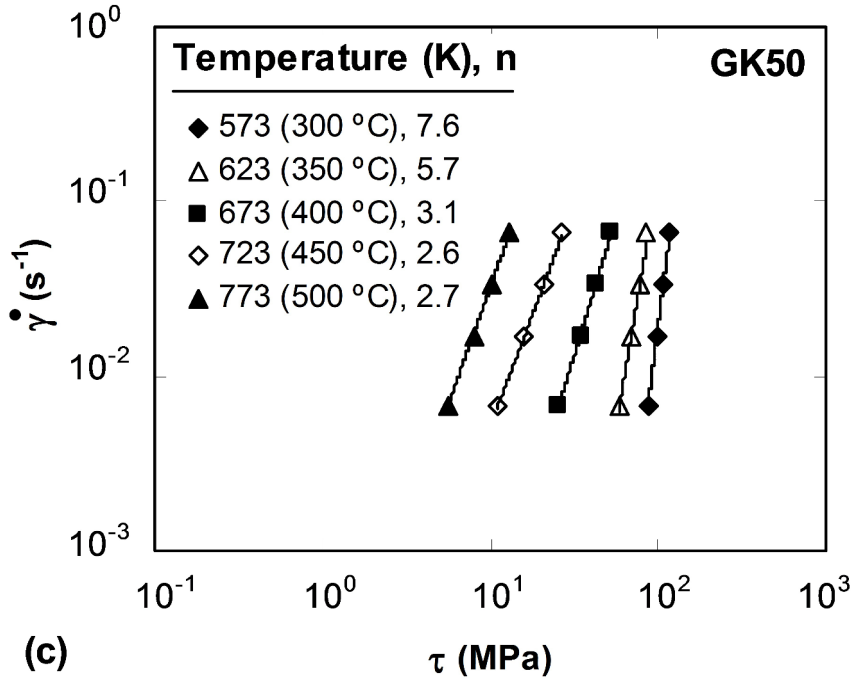
Temperature (K), n
GK50
573 (300 °C), 7.6
623 (350 °C), 5.7
673 (400 °C), 3.1
723 (450 °C), 2.6
773 (500 °C), 2.7
$\dot{\gamma}$ (s^{-1})
10^{0}
10^{-1}
10^{-2}
10^{-3}
10^{-1}
10^{0}
10^{1}
10^{2}
10^{3}
τ (MPa)

(c)

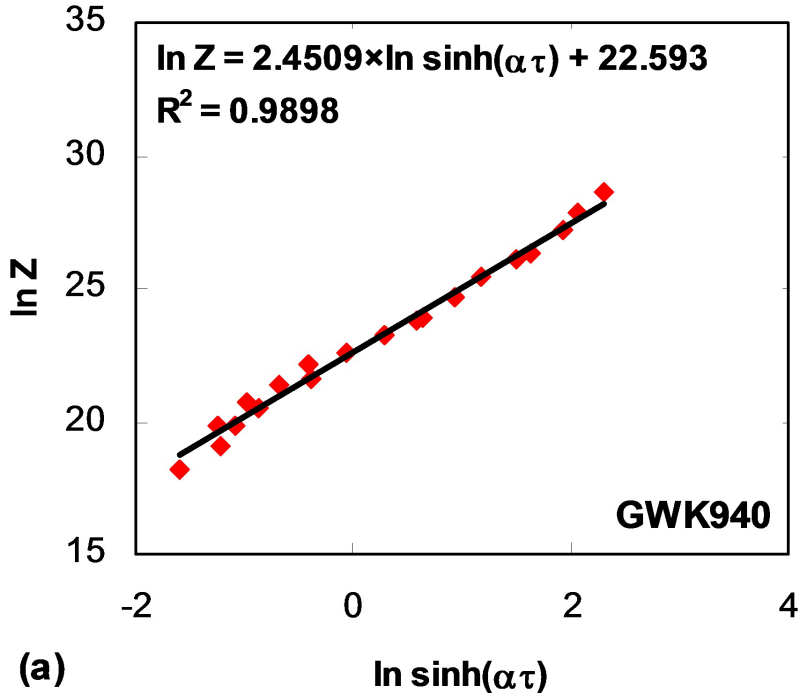
ln Z = 2.4509×ln sinh(ατ) + 22.593
R² = 0.9898
GWK940
ln Z
ln sinh(ατ)
35
30
25
20
15
-2
0
2
4

(a)

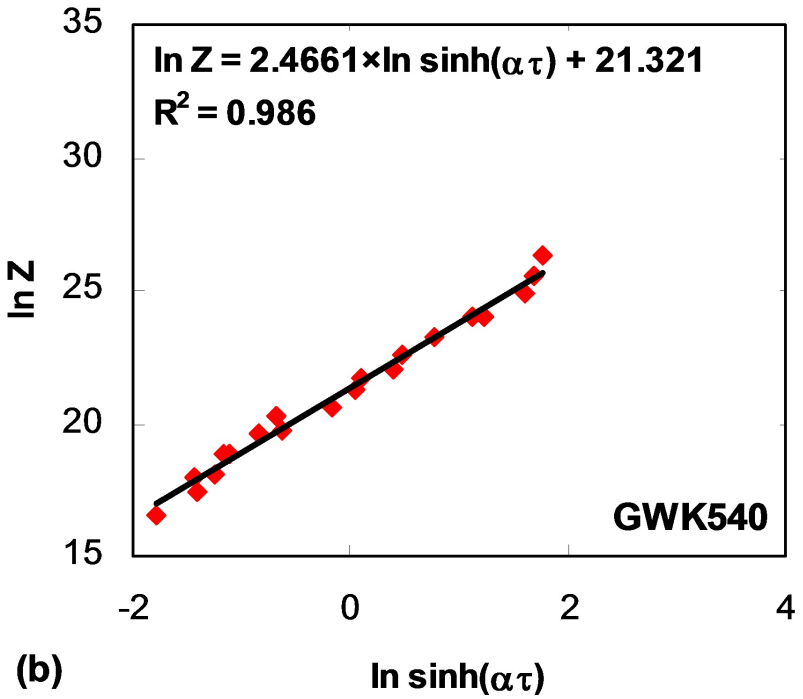
ln Z = 2.4661×ln sinh(ατ) + 21.321
R² = 0.986
GWK540
ln Z
ln sinh(ατ)
35
30
25
20
15
-2
0
2
4

(b)

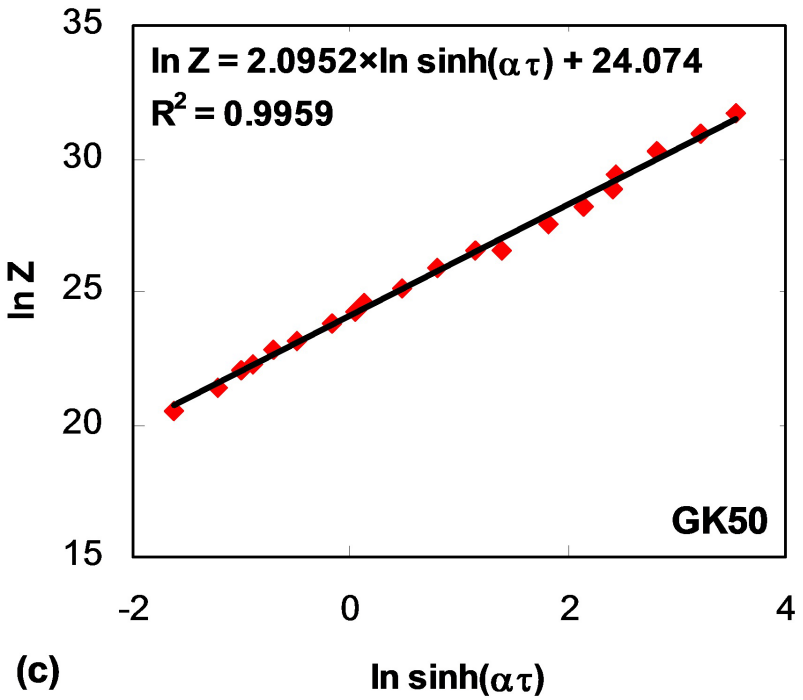
ln Z = 2.0952×ln sinh(ατ) + 24.074
R² = 0.9959
GK50
ln Z
ln sinh(ατ)
35
30
25
20
15
-2
0
2
4

(c)

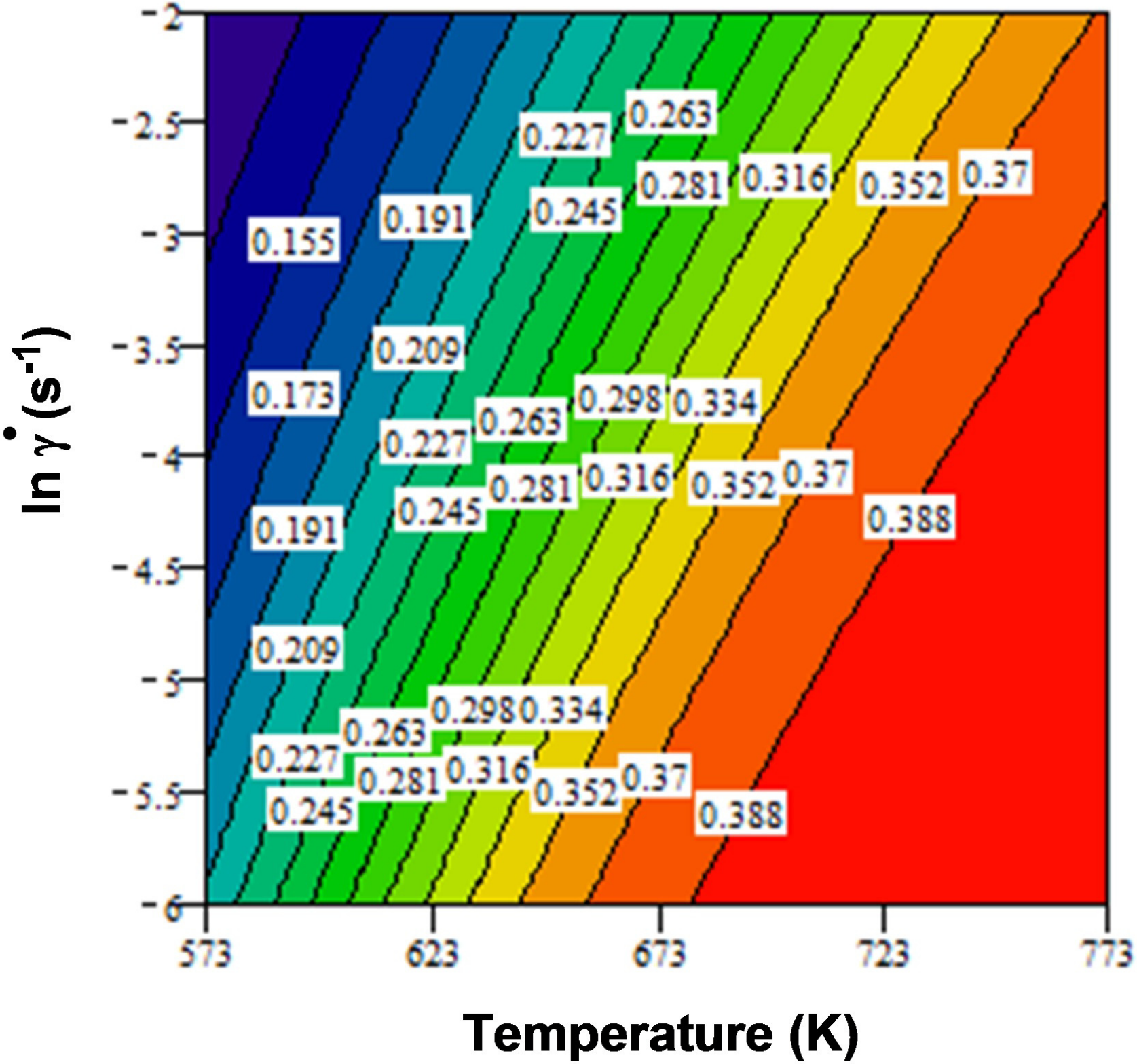
-2
-2.5
-3
-3.5
-4
-4.5
-5
-5.5
-6
ln $\dot{\gamma}$ (s^{-1})
573
623
673
723
773
Temperature (K)
0.155
0.191
0.209
0.173
0.227
0.263
0.298
0.334
0.245
0.281
0.316
0.352
0.37
0.388

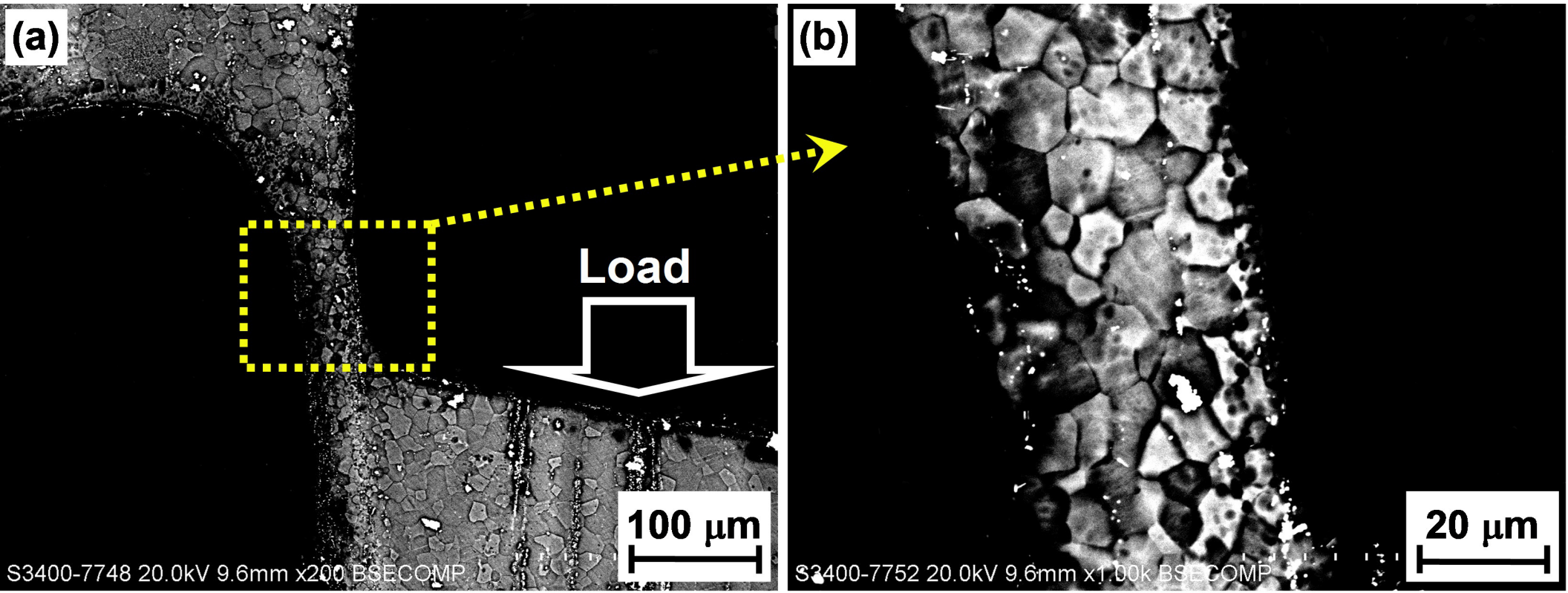
(a)
Load
100 μm
S3400-7748 20.0kV 9.6mm x200 BSECOMP
(b)
20 μm
S3400-7752 20.0kV 9.6mm x1.00k BSECOMP

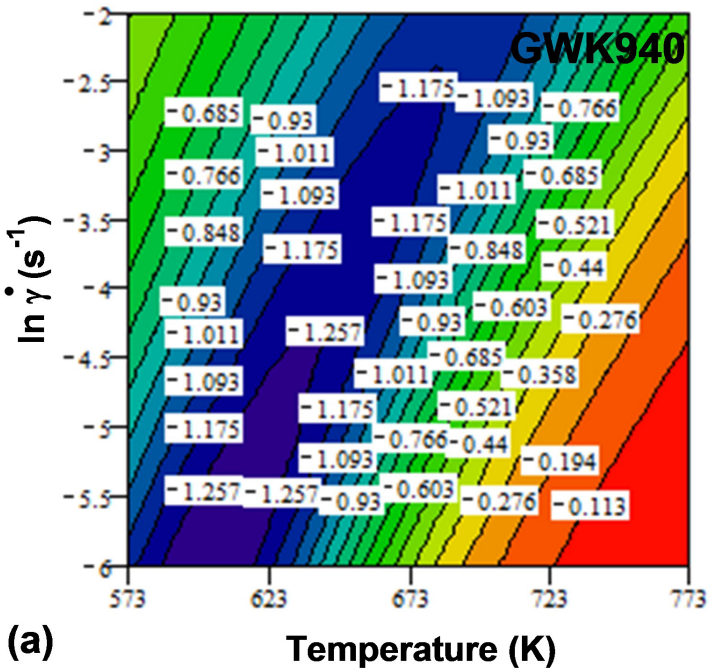
GWK940
ln $\dot{\gamma}$ (s^{-1})
Temperature (K)
573
623
673
723
773
-2
-2.5
-3
-3.5
-4
-4.5
-5
-5.5
-6
-0.685
-0.93
-1.011
-0.766
-1.093
-0.848
-1.175
-0.93
-1.011
-1.257
-1.093
-1.175
-1.257
-1.257
-0.93
-1.175
-1.093
-1.011
-0.93
-0.766
-1.093
-0.848
-1.175
-0.685
-1.011
-0.521
-0.93
-0.848
-0.44
-1.093
-0.603
-0.276
-0.685
-1.011
-0.358
-0.521
-1.175
-0.766
-0.44
-1.093
-0.194
-0.603
-0.276
-0.113

(a)

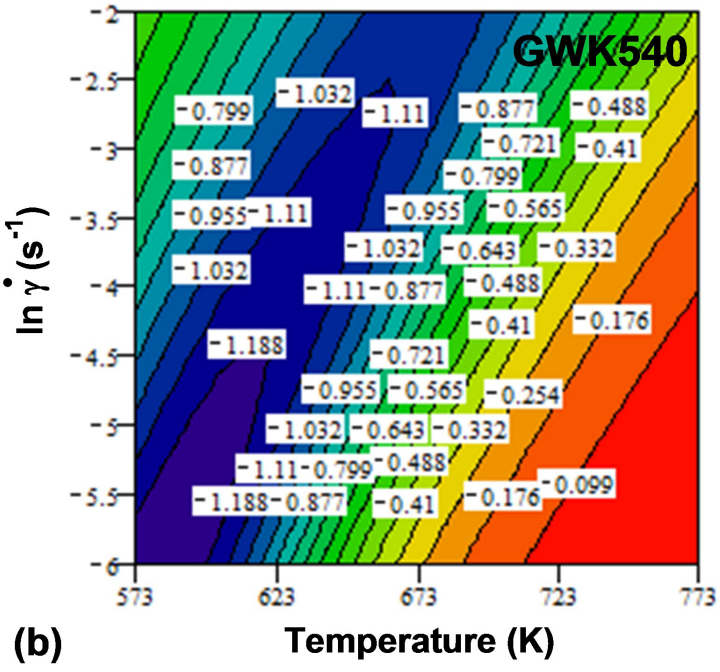
GWK540
ln $\dot{\gamma}$ (s^{-1})
Temperature (K)
573
623
673
723
773
-2
-2.5
-3
-3.5
-4
-4.5
-5
-5.5
-6
-0.799
-1.032
-1.11
-0.877
-0.488
-0.877
-0.721
-0.41
-0.955
-1.11
-0.799
-0.955
-0.565
-1.032
-0.643
-0.332
-1.11
-0.877
-0.488
-1.188
-0.41
-0.176
-0.955
-0.721
-0.565
-0.254
-1.032
-0.643
-0.332
-1.11
-0.799
-0.488
-1.188
-0.877
-0.41
-0.176
-0.099

(b)

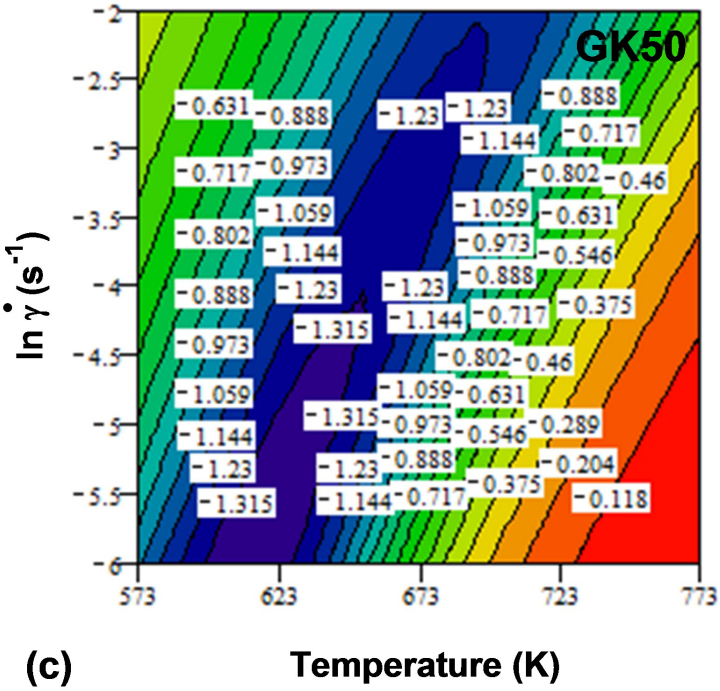
GK50
ln $\dot{\gamma}$ (s^{-1})
Temperature (K)
573
623
673
723
773
-2
-2.5
-3
-3.5
-4
-4.5
-5
-5.5
-6
-0.631
-0.888
-1.23
-1.23
-0.888
-1.144
-0.717
-0.717
-0.973
-0.802
-0.46
-1.059
-1.059
-0.631
-0.802
-1.144
-0.973
-0.546
-0.888
-1.23
-1.23
-0.888
-1.315
-1.144
-0.717
-0.375
-0.973
-0.802
-0.46
-1.059
-1.059
-0.631
-1.315
-0.973
-0.546
-0.289
-1.144
-1.23
-0.888
-0.204
-1.23
-1.144
-0.717
-0.375
-1.315
-0.118

(c)

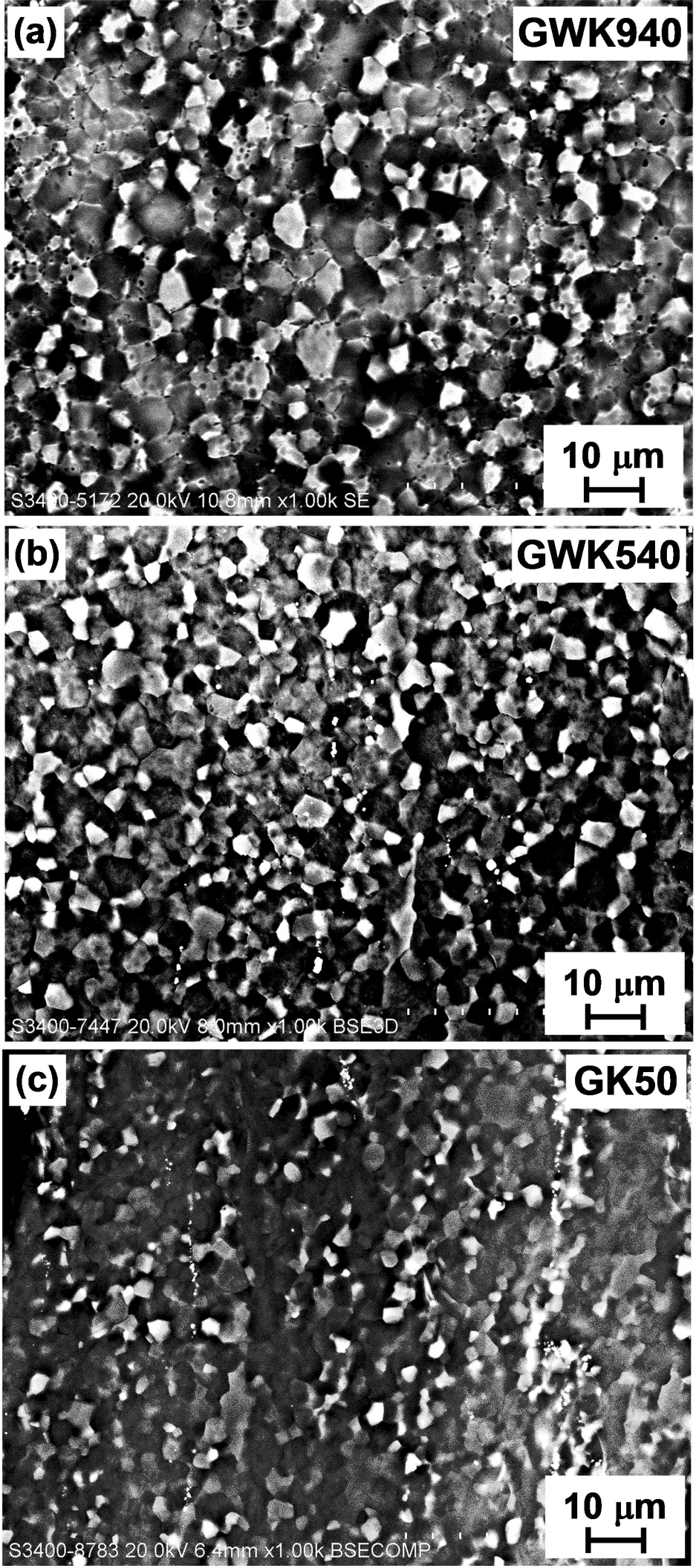
(a)
GWK940
10 μm
S3400-5172 20.0kV 10.8mm x1.00k SE
(b)
GWK540
10 μm
S3400-7447 20.0kV 8.0mm x1.00k BSE3D
(c)
GK50
10 μm
S3400-8783 20.0kV 6.4mm x1.00k BSECOMP

Table I. Summary of Literature Data on the Hot deformation Analysis of Mg–Gd–Y–Zr alloys

Alloy	Initial condition		Compression test conditions		Constitutive equation parameters				Reference
	Process	Grain size (μm)	Temperature (K)	Strain rate (s^{-1})	A (s^{-1})	α (MPa^{-1})	n	Q (kJ/mol)	
Mg–7Gd–5Y–1.2N–1Zr	AC[1]	-	573-723 (300-450 °C)	0.002-1	2.40×10^{15}	0.017	3.2	234	[11]
Mg–10Gd–3Y–0.5Zr	C+H[2]	-	573-723 (300-450 °C)	0.001-1	3.70×10^{21}	0.01	5.4	309	[12]
Mg–9.3Gd–2.9Y–0.35Zr	C+H	-	573-723 (300-450 °C)	0.001-1	3.3×10^{17}	0.042	5.0	252	[13]
Mg–6.85Gd–4.52Y–1.15Nd–0.55Zr	C+H	200	623-803 (350-530 °C)	0.005-5	1.07×10^{16}	0.016	3.7	250	[14]
Mg–8.90Gd–5.11Y–3.10Zn–0.47Zr	EX[3]	9.8	573-773 (300-500 °C)	0.001-1	2.68×10^{16}	0.011	3.9	240	[15]
Mg–11Gd–2Y–1Zn–1Zr	C+H	-	623-753 (350-480 °C)	0.001-0.5	3.18×10^{18}	0.009	6.8	273	[16]
Mg–9Gd–4Y–0.6Zr	C+H	100	623-773 (350-500 °C)	0.001-1.0	1.22×10^{5}	0.007	4.3	209	[17]
Mg–9.8Gd–2.7Y–0.4Zr	EX	-	648-723 (375-450 °C)	0.01-5	1.94×10^{16}	0.009	4.3	229	[18]

[1] As-cast
[2] Cast and homogenized
[3] Extruded